

Quantitative modeling of *in situ* x-ray reflectivity during organic molecule thin film growth

A. R. Woll,¹ T. V. Desai,² and J. R. Engstrom²

¹*Cornell High Energy Synchrotron Source,
Cornell University, Ithaca, NY 14853, USA*

²*School of Chemical and Biomolecular Engineering,
Cornell University, Ithaca, NY 14853, USA*

(Dated: July 19, 2022)

Abstract

Synchrotron-based x-ray scattering is increasingly employed as an *in situ* probe of structure, morphology, and kinetics during thin film growth. A simple, but widely used approach is to monitor the scattered intensity at a particular position in q-space, typically the so-called “anti-Bragg” position. This intensity provides immediate information about the evolution of surface morphology. However, interpreting such data can be complicated by details of the system, such as the presence of buried interfaces on the substrate and dependence of growth rate on coverage. Accounting for such details, in order to obtain quantitative details about the surface morphology, requires modeling the growth process. Although a variety of suitable models have been developed and employed, virtually no general information concerning their scope or accuracy exists in the literature. Of particular importance is the accuracy with which layer coverages can be extracted from fits of such models to reflectivity data. Here, after briefly reviewing the relevant x-ray scattering calculations, we present a detailed comparison of three of these models. Using experimental data obtained from hyperthermal deposition of pentane and diindenoperylene (DIP) on SiO₂, we compare and contrast these models, both with each other and with detailed characterization of the surface morphology using ex-situ atomic force microscopy (AFM). We find that the surface morphology obtained from fits to the *in situ* x-ray data compare well with the actual morphology at early times, independent of which model is used. This agreement deteriorates at later time, once the root-mean squared (rms) film roughness exceeds about 1 ML. Nevertheless, interesting differences among the models exist. For pentacene/SiO₂, which exhibits rapid roughening near completion of the second layer, the different models obtain different growth rates. Also, because layer coverages are under-determined by the evolution of a single point on the reflectivity curve, χ^2 is a useful but insufficient measure of the accuracy of the model. Instead, it appears more important that the model reproduce each of the extrema in the data. Two of the models described here include explicit representations of underlying, kinetic parameters of the system. Having established that these models may be used to extract the surface morphology of a growing thin film with reasonable accuracy, we discuss the prospect of validating the correspondence between model parameters and real, kinetic parameters of a system.

PACS numbers: Valid PACS appear here

I. INTRODUCTION

In situ, surface-sensitive scattering techniques, such as RHEED and x-ray scattering at the so-called “anti-Bragg” position^{1–3}, have been widely applied to virtually all thin film growth techniques—such as electrodeposition⁴, MBE, CVD^{5,6}, and PLD^{7–12}. Their principal advantages, compared to microscopy-based techniques such as AFM and STM, are their versatility, time resolution, and the fact that such techniques provide direct information about surface morphology during growth. For example in homoepitaxy, growth is classified as “step-flow” (SF), “layer-by-layer” (LBL) or “three-dimensional” based, respectively, on whether the specular reflectivity remains constant, oscillates, or decreases monotonically with increasing film thickness. An additional advantage of x-ray scattering is the accuracy with which precise calculations of scattered intensity can be performed. Increasingly, this has been exploited^{13,14} to extract quantitative information about the surface morphology, namely the layer coverages as a function of time $\theta_n(t)$, during growth. This analysis, however, requires a specific model of the morphological evolution of the film. A variety of models have been employed for this purpose, yet there appears to be little or no detailed comparisons of these models in the literature. Moreover, the accuracy with which this type of analysis reproduces thin film morphology has not been explicitly evaluated.

Figure 1 shows x-ray reflectivity (XRR) and AFM data obtained from four pentacene films, grown in immediate succession on a single SiO₂ substrate under nominally identical conditions (substrate temperature 40°C), and serves to illustrate the main subject of this work: how accurately can height distributions, which may be obtained directly from the AFM data in Fig. 1B-E, be extracted from fits to the x-ray data in Fig. 1A? In addition, how does the choice of model used for such analysis affect the simulated morphology?

The models described here are necessary, in part, because the x-ray intensity measurements such as those in Figure 1A are performed at only one point in reciprocal space. As has recently been demonstrated^{15–19}, measuring multiple points along the reflectivity curve can reduce or potentially obviate the requirement for such models. However, such measurements are not always possible or compatible with a particular system or experiment. Further, with notable exceptions¹⁹, such enhanced measurements are often used not to replace the use of growth models, but to limit uncertainties associated with comparing measurements to calculations. Finally, although this manuscript deals with the limited problem of determining

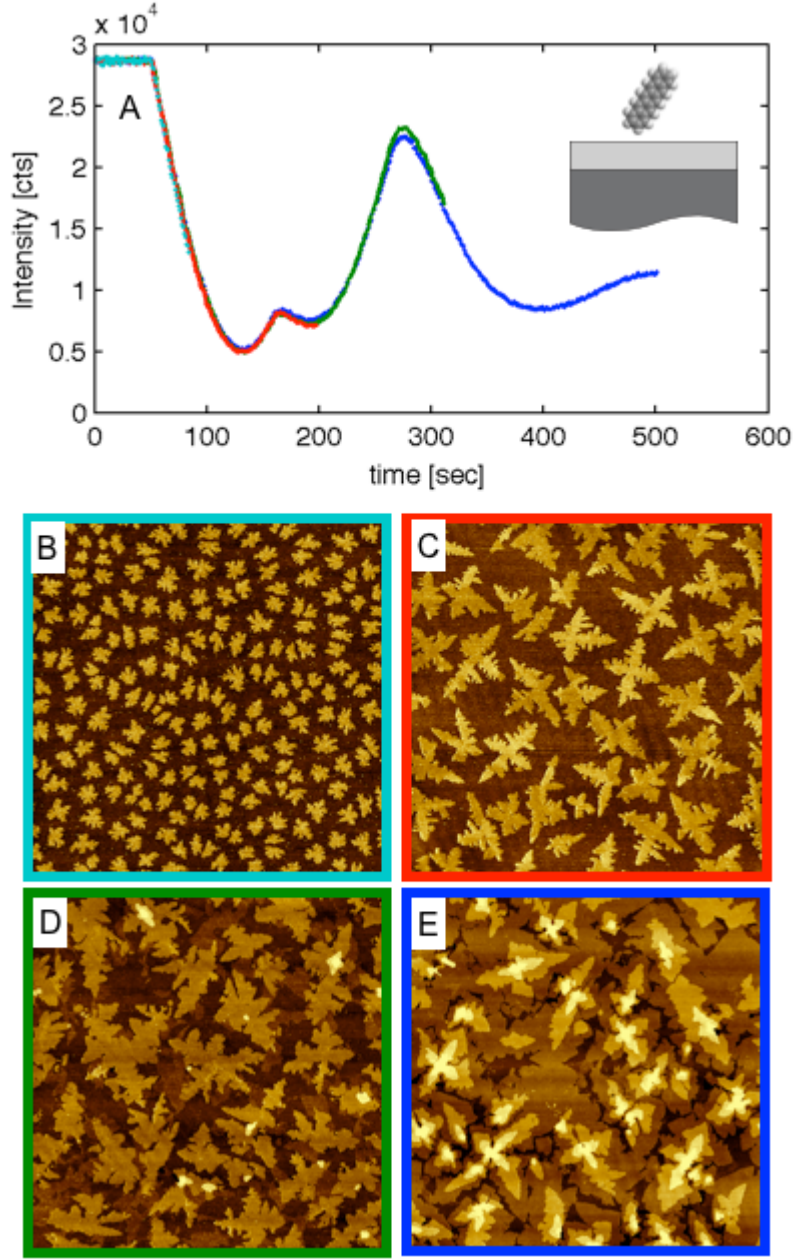


FIG. 1: (A) X-ray reflectivity data obtained near the pentacene anti-Bragg position during pentacene deposition on SiO_2 . Data from four separate growths-performed in immediate succession on the same substrate and under the same conditions except growth time-are shown. (B-E) AFM images of the four pentacene/ SiO_2 thin films represented in (A): (B) 0.34 ML; (C) 1.4 ML; (D) 2.5 ML; (E) 4.4 ML. All images are $20\text{ }\mu\text{m} \times 20\text{ }\mu\text{m}$.

the surface morphology of a growing film, the models described here concern the broader challenge of understanding, in detail, how microscopic, kinetic parameters of a system determine its morphology. Clearly, comparing the simulated morphologies of these models to real systems is a critical, first step in validating them for deeper, more general use.

One motivation for this work is to evaluate a particular model (the “modified Cohen” model, see section III B below) we recently developed to measure the time-dependent growth rate of hyperthermally-deposited organic thin films²⁰. This time-dependence arises from differences between the sticking probabilities of deposited molecules, depending on whether the molecules land onto the bare substrate or the growing film. Because this sticking probability depends strongly on the substrate, a quartz crystal monitor is an inappropriate measure of growth rate. This phenomena has been observed in other systems: in metal-organic based GaN MBE on sapphire, both growth rate acceleration¹⁴ and deceleration²¹ have been observed using in situ measurements of Ga $K\alpha$ x-ray fluorescence. For organic molecules containing only light elements, this method is not possible. Growth rate acceleration may also be determined using ex situ microscopy (see section IV B below), but this approach requires several samples per growth condition, and can be severely complicated by the presence of de-wetting, a common phenomena in organic thin films²². Accurate determination of growth rates and growth rate acceleration from time-resolved XRR data relies directly on quantitative analysis as described above, and thus on the ability of models to reproduce the distribution of layer coverages as a function of time. In prior studies, we validated this approach by comparing both the total film thickness and rms roughnesses of thin films measured by AFM to those predicted by best-fit simulations. However, a detailed description of the model we employed was beyond the scope of those publications. Here, we provide a complete description of this model, and also address the specific problem of measuring growth rate acceleration: namely, how accurately can growth rates and growth rate acceleration be measured by quantitative analysis of in situ XRR data?

We proceed by comparing three distinct deterministic, rate-equation models to two particular systems. The first of these, pentacene/ SiO_2 (represented in Figure 1), serves as a particularly simple model system: its structural and morphological evolution is well known and, under these growth conditions (see section IV A), does not exhibit growth rate acceleration. Four films of varying film thickness are grown under identical conditions. We compare height distributions measured with AFM to those deduced using fits to reflectivity

data at the anti-Bragg position. We find that distinct models each fit the data well by eye, but do not constitute complete descriptions of the data in the chi-squared sense. In other words, when the measurements are obtained with very good statistics ($\lesssim 1\%$), our model does not account for all of the variation in the data. Nevertheless, the height distributions obtained for these films from AFM agree well with those predicted by all three models. We thus conclude that “reasonable” fits to data—those that reproduce the most conspicuous features of the data—generally provide reasonably accurate layer coverages. The second system described in this paper, diindenoperylene (DIP)/SiO₂, exhibits growth rate acceleration, which we model as a difference in sticking coefficient on the substrate and on deposited film. We find that two of the models, including that in Ref. 20, accurately describe the degree of acceleration, corroborating results reported therein.

II. EXPERIMENTAL

Experiments were conducted at the G3 station at the Cornell Higher Energy Synchrotron Source (CHESS) in a custom-designed, ultrahigh vacuum chamber with a base pressure of 4×10^{-9} Torr described previously^{20,23}. Growth was performed on 300 nm-thick SiO₂ thermal oxide films on Si(001) wafers, using a hyperthermal molecular source. The deposition energy, measured using time-of-flight mass spectrometry, was approximately 2.5 eV for pentacene and 4.2 eV for DIP. Synthetic W/B₄C multilayer monochromators set the beam energy to 9.75 keV with $\Delta E/E = 1.5\%$. The unattenuated flux at the sample position was approximately 5×10^{13} photons-s⁻¹-mm⁻². In order to avoid radiation damage, the beam was attenuated by a factor of 10 or more using multiple layers of aluminum foil at the upstream end of the hutch. An avalanche photodiode detector (Oxford Danfysik, Oxford, UK) scintillator counter was used for measuring the scattered x-ray intensity. AFM was conducted ex situ in tapping mode using a Digital Instruments 3100 Dimension microscope (Santa Barbara, CA).

III. THEORY

A. X-ray Scattering

The computational simplicity of x-ray scattering results from the fact that, far from a Bragg peak or from the critical angle for total external reflection, the single scattering (kinematic) approximation may be used²⁴. In this approximation, the scattered intensity is $I(\vec{q}) = F(q_z)|A(\vec{q})|^2$,²⁴ where the scattering amplitude $A(\vec{q})$ is the Fourier transform of the electron density:

$$A(\vec{q}) = \int_V \rho(\vec{r}) \exp(-i\vec{q} \cdot \vec{r}). \quad (1)$$

For the particular case of in situ data collected during thin film growth at a position q_z in reciprocal space, and with the assumption that the substrate does not vary during deposition, this may be simplified to^{14,18,25},

$$I(q_z, t) \propto |A(q_z, t)|^2 = \left| A_{\text{sub}} e^{i\phi_{\text{sub}}} + A_{\text{film}} \sum_{n=1} \theta_n(t) e^{-iq_z c(n-1)} \right|^2. \quad (2)$$

Here, θ_n is the fractional coverage of layer n , c is the lattice parameter of the film normal to the surface, and A_{film} and A_{sub} are both defined as pure real. Thus there are only two unknown scattering parameters, ϕ_{sub} and ratio of scattering amplitudes $A_{\text{film}}/A_{\text{sub}}$. These parameters are often treated as free parameters in the fit. However, it is often useful to constrain them using known parameters of the system without resorting to full, atomic-scale models of $\rho(\vec{r})$. For large, organic molecules, the anti-Bragg position probes an approximate length scale $l = 2\pi/q_z = c/L$, which is large compared to interatomic distances. As a result, a molecular layer is well approximated by a uniform density slab. In appendix A we derive a general expression for A_{sub} and ϕ_{sub} under the assumption that the sample geometry resembles that of Fig. 2. Specifically, we assume that the substrate is composed of a thin amorphous layer with density ρ_1 and thickness $T_1 = c\tau$ on an amorphous, semi-infinite layer with density ρ_0 . For organic thin film growth, common substrates that may be described by this model include crystalline Si substrates with a thin SiO₂ native oxide²⁶, and thick, thermal SiO₂ layers covered by a self-assembled monolayer^{22,27} or an interfacial water layer^{25,28}. In the approximation that the film is also composed of uniform density layers having density ρ_2 , we have the result

$$A_{\text{sub}} = \frac{2\pi}{cL} i e^{i\pi L(1+2\Delta)} (\rho_1 + (\rho_0 - \rho_1) e^{i2\pi L\tau}), \quad (3)$$

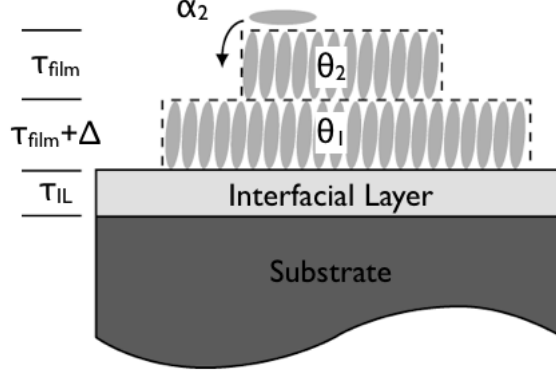


FIG. 2: Real-space schematic representation of organic thin film growth.

such that ϕ_{sub} is simply the complex phase of A_{sub} in Eq. 3, while $A_{\text{film}}/A_{\text{sub}}$ becomes

$$\frac{A_{\text{film}}}{A_{\text{sub}}} = \frac{2\rho_2 \sin \pi L}{|\rho_1 + (\rho_0 - \rho_1)e^{i2\pi L\tau}|}. \quad (4)$$

In Eqs. 3 and 4, $L = q_z/(2\pi/c)$ is q_z in reciprocal lattice units of the deposited film, and Δ corresponds to a small difference, as a fraction of unit cell height c , in height of the center of the first deposited layer from $c/2$ above the substrate surface.

Despite the fact that Eqs. 3 and 4 include more than the two, original parameters in Eq. 2, this representation generally reduces parameter space, since these parameters are at least approximately known, and can thus be constrained in the fit. To help interpret Equation 2, the complex scattering amplitudes A_{sub} and A_{film} are represented schematically in the Fig. 3. In addition, this figure shows the two components of A_{sub} , A_1 and A_2 , the scattering amplitudes of the semi-infinite substrate and interfacial layer. This representation allows visualization of the behavior of anti-Bragg intensity oscillations during heteroepitaxial, LBL growth, as has been described previously by Kowarik et al¹⁸. Considering ideal LBL growth: as the coverage of the first film layer θ_1 increases from 0 to 1, the total scattering amplitude moves from the tip of A_{sub} to the tip of A_{film} in Fig. 3. Since the next layer is out of phase with the first, it contributes a term $-A_{\text{film}}\theta_2$ to the scattering amplitude, so that the total amplitude moves back towards the tip of A_{sub} . Thus, the magnitude of the total complex amplitude traverses minima at fractional coverages and maxima at the coverage of each completed layer. However, the relative height of the maximum corresponding to layer completion depends on both $A_{\text{film}}/A_{\text{sub}}$ and ϕ_{sub} . Also, if ρ_2 is sufficiently small, a single layer completion will correspond to an intensity minimum rather than a maximum. For

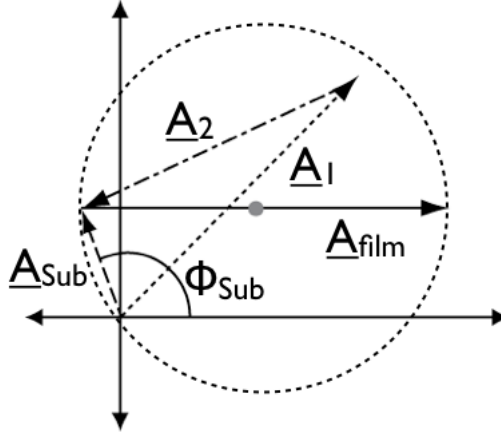


FIG. 3: Complex Scattering amplitude of a growing film.

non-ideal LBL growth, the total scattering amplitude is still confined to the line segment between $A_{\text{sub}}\phi_{\text{sub}}$ and $A_{\text{sub}}\phi_{\text{sub}} + A_{\text{film}}$. However, local maxima no longer necessarily correspond to integer coverage. Deviations from this correspondence result, in general, from the development of an asymmetric surface morphology²¹.

Also indicated, as a filled circle in Fig. 3, is the position corresponding to 0.5 ML coverage of a single layer, the mid-point of segment A_{film} . The significance of this point is that it also corresponds to the final scattering amplitude of the sample once the film surface has become rough compared to c . This conclusion is reached by summing the series on the right hand side of Eq. 2 assuming a large number of layers with slowly decreasing θ_n , e.g. $\theta_n = \exp(-\delta n)$, corresponding to a rough film/vacuum interface. The resulting, total scattering amplitude of the film is $A_{\text{film}}/2$. In other words, the scattering amplitude, at the anti-Bragg position, of a film with a smooth substrate film interface but rough top surface is precisely half that of a single ML of material.

Finally, although not applicable to organic thin film growth on amorphous substrates, we note that the representation in Fig. 3 may also be used to visualize the distinction between so-called “roughness” and “Keissig” oscillations associated with LBL growth and step-flow (SF) growth, respectively. It has often been noted, for example, that LBL growth can give rise to one intensity maximum per monolayer at the anti-Bragg positions, whereas SF growth exhibits one maximum every two layers^{12,29}. In appendix B we show that during SF growth, the total scattering amplitude at the anti-Bragg position traverses the dashed circle once every two monolayers. This construction clearly accounts for the difference in periodicity

between LBL and SF growth. It also shows that oscillation maxima during SF growth need not occur at integer coverage.

The construction in Fig. 3 can be generalized to visualize the scattering amplitude at reciprocal space positions other than the anti-Bragg. Kowarik et al¹⁸ have already noted that at particular fractional values of L , the scattering amplitude of the film during LBL growth traverses regular, convex polygons in the complex plane, e.g. a triangle at $L = 2/3$. More generally, this amplitude traverses a regular, but not necessarily convex, polygon. During SF growth (see appendix B), the scattering amplitude traverses the circle which inscribes the shape that would be traced in LBL growth, with a period of $1/L$. Clearly, ideal LBL and SF growth have identical scattering amplitudes at integer layer thicknesses.

B. Layer-wise Rate Equation Model of Epitaxial Growth

Even if the scattering parameters described in section III A are precisely known, it is clear that the coverages $\theta_n(t)$ at time t are not uniquely determined by a single intensity value $I(t)$. To determine these coverages, additional information about the surface evolution is required. The most common approach is to construct a deterministic, parameterized model for the evolution of coverages $\theta_n(t)$. Such models take the form of coupled, differential equations:

$$\frac{d\theta_n}{dt} = F(k_j, \dots, \theta_{n-1}, \theta_n, \theta_{n+1}, \dots, t), \quad (5)$$

where the functions F represent the “additional information” about growth imposed on the system, and may or may not depend explicitly on a subset of coverages and time t . The parameters k_j determine the $\theta_n(t)$ ’s, which are substituted into Eq. 2 to calculate $I(t)$.

We note that a large variety of models of the form in Eq. 5 have been developed over the last several decades. Most of these originated and evolved in the context of specific experimental techniques, such as Auger Electron Spectroscopy (AES)^{30–33}, ion-beam assisted deposition^{34–36}, and Reflection High Energy Electron Diffraction (RHEED)^{37,38}. Models used to analyze XRR data^{13,14,18,20,25} as described here have virtually all drawn directly from those of Ref.[37]. More recently, Trofimov et al^{39–43}, developed a new variant of this class of models, specifically for the purpose of linking atomistic kinetics to morphology in thin, multilayer films.

It is convenient to categorize these models according to how much they attempt to incor-

porate atom-level kinetics. Models by Kariotis et al³⁸, Trofimov et al^{39–43}, and Koponen^{34,35} draw directly on well-known sub-monolayer nucleation theory⁴⁴, and include additional equations to Eq. 5 representing the adatom and island densities on each layer. The next simplest models, most notably those introduced by Cohen et al³⁷, but including Refs.[32,33,36], do not explicitly attempt to model atom-level kinetics, but approximate these kinetics in the form of Eq. 5. For example, the “distributed” model described in Ref.[37] includes a mean-field representation of the step-density of a layer as a function of coverage θ , which in turn controls the amount of downhill interlayer diffusion. Finally, Braun et al¹⁵ have developed a version of Eq. 5 which attempts, explicitly, to avoid modeling atomistic kinetics. Rather, the equations Eq. 5 are coupled via intermediate functions $J_n(t)$, chosen to be as simple as possible consistent with producing physically reasonable results for the functions $\theta_n(t)$.

Below, we implement three of the models described above: the empirical model described by Braun et al¹⁵, a simplified version of the model introduced by Trofimov et al³⁹, and our variant^{20,22,45} of the distributed model introduced in Ref.[37]. In each case, we introduce analogous modifications that were found necessary to fit data obtained for our model systems, pentacene/SiO₂ and DIP/SiO₂. Specifically, successful fits require that the kinetic parameters change with layer number for at least the first three layers. For the case of DIP/SiO₂, it is additionally required that the sticking coefficient of incident molecular species vary with coverage of the first layer. After describing our model in detail, we also describe our implementations of the models Refs.[15] and [39] for the analysis in section II.

First, we present two modifications to the so-called “distributed” model of Ref.[37] that widen its range of applicability and connect, within the limits of the mean-field approach, to well-defined physical quantities. The model, (depicted schematically in Fig. 2), is written:

$$\frac{d\theta_n}{dt} = R_n (1 - \alpha_{n-1}) (\theta_{n-1} - \theta_n) + R_{n+1} \alpha_n (\theta_n - \theta_{n+1}), \quad (6)$$

where R_n and α_n are the net deposition rate from vapor and downward interlayer transport probability into the n^{th} layer. The parameters R_n and α_n implicitly represent all of the kinetic processes involving molecular attachment and transport, respectively. Rather than Cohen’s original form for α_n , we use

$$\alpha_n(\theta_n, \theta_{n+1}) = \frac{k_- d(\theta_n)}{k_- d(\theta_n) + k_+ d(\theta_{n+1})} = \frac{e^{-E'} d(\theta_n)}{e^{-E'} d(\theta_n) + d(\theta_{n+1})}, \quad (7)$$

where $d(\theta)$ represents the average step-edge density of a with coverage θ . The factors $k_{-(+)}$ represent the rate of molecular attachment at downhill (uphill) steps, and $e^{-E'} =$

k_-/k_+ . The ratio k_-/k_+ , in the assumption of irreversible attachment, is proportional to $\exp(-E_{ES}/kT)^{46}$. In general, the function $d(\theta)$ could depend on layer number, for example if the island density changes as a function of layer thickness or island shape. Since such differences are virtually indistinguishable from differences in E' , we use the same function $d(\theta)$ for each layer, but typically allow variations in E' as a function of n .

The rate equations described by Equation 5 do not explicitly prevent overhangs, i.e. solutions in which $\theta_n(t) > \theta_{n-1}(t)$ for some n and t . Overhangs can occur, for example, if $E_2 \ll E_1$, so that the interlayer transport into layer 2 is much greater than the transport of layer 2 into layer 1. In our implementation of the Cohen model, overhangs are prevented by forcing α_n to approach 0 as θ_n approaches θ_{n-1} .

The parameterization in Eq. 7 fixes a drawback of the original form, in which α_n is defined as³⁷ $\alpha_n = Ad(\theta_n)/(d(\theta_n) + d(\theta_{n+1}))$. In this case, $A = 1$ corresponds to $E' = -\infty$ in our model, whereas $0 \leq A < 1$ corresponds, approximately, to $E' > 0$. The region that is mathematically forbidden in Cohen's original form, $-\infty < E \leq 0$, is precisely the region of parameter space where extended LBL oscillations are expected. As noted in Ref. 37, that model is unable to reproduce such behavior.

Our second modification to the Cohen model is to employ recent work of Tomellini et al⁴⁷ concerning the form of $d(\theta)$: the mean-field step-edge density of a growing film comprised of 2D islands. Two forms of $d(\theta)$ are obtained, depending on whether or not islands rearrange when they merge, reducing their total perimeter. The zero and complete rearrangement limits are labeled “impingement” and “coalescence” regimes, respectively, and are found to have step densities d_{im} and d_{co} ⁴⁷:

$$d_{\text{im}}(\theta) = 2\sqrt{\pi N_0}(1 - \theta) \left[\ln \frac{1}{(1 - \theta)} \right]^{1/2}, \text{ and} \quad (8)$$

$$d_{\text{co}}(\theta) = \sqrt{\theta(1 - \theta)} \exp \left(-\frac{\theta}{2(1 - \theta)} \right). \quad (9)$$

Eq. (9) reflects the fact that if islands rearrange upon coalescence, the density of holes remaining in the surface near layer completion is smaller than the island density at nucleation. This implies that the step-edge density is also smaller, e.g. $d(1 - \epsilon) \ll d(\epsilon)$. Real systems are expected to exhibit behavior intermediate between that of Eqs. (8) and (9). In practice, we parameterize this form so that the degree of coalescence may be tuned by a parameter δ , $0 \leq \delta \leq 1$:

$$d(\theta) = \delta d_{\text{co}}(\theta) + (1 - \delta) d_{\text{im}}(\theta). \quad (10)$$

In order to solve (6) using (7) and (10), it is necessary to “nucleate” layers 2 and above, since α_n otherwise remains equal to one, precluding nucleation of layer $n + 1$. This is done by computing $d(\theta_{n+1})$ using a small value ($\epsilon \sim 10^{-5}$) of θ_{n+1} when θ_n exceeds a critical coverage $\theta_{n,\text{cr}}$. Explicitly:

$$\alpha_n = \begin{cases} 1, & \theta_n < \theta_{n,\text{cr}} \\ \alpha_n(\theta_n, \theta_{n+1} + \epsilon), & \theta_n \geq \theta_{n,\text{cr}}. \end{cases} \quad (11)$$

Using Eqs. 7 and 10, we find that the results obtained by numerically solving Eq. 6 may be tuned, via the parameter E' , from 3D growth ($E' \gg 1$) to perfect LBL growth ($E' \ll -1$). More complicated behavior can result from allowing different values of E' for different layers. For pentacene deposition on SiO_2 , we find that reasonable results (discussed further in section II) are obtained by employing several values of E' , e.g. E_1, E_2 for the first two layers, followed by asymptotic approach to $E_2 + \Delta E_N$ for layers $n \geq 3$, e.g. $E_{n \geq 3} = E_2 + \Delta E_N \times \exp((n - 2)/N_0)$. For DIP/ SiO_2 and other systems exhibiting growth rate acceleration, R_1 is allowed to differ from $R_{n>1}$, simulating a difference in sticking coefficient for molecules incident on the growing film as opposed to the bare substrate. In summary, then, our model for real systems involves ten growth parameters, $R_1, R_{n>1}, E_1, E_2, \Delta E_N, \theta_{1,\text{cr}}, N_0, \theta_{2,\text{cr}}, \theta_{N,\text{cr}}$, and δ .

As described briefly above, the model introduced by Ref.[15] is simpler than those described in Ref.[37]. Equation 5 takes the form:

$$\frac{d\theta_n}{dt} = R_n(J_n - J_{n+1}), \quad (12)$$

where the intermediate functions J_n depend explicitly on time as

$$J_n = \frac{1}{2} \left(1 + \tanh \left(\frac{t - t_n}{\beta_n} \right) \right). \quad (13)$$

Here, the times t_n are determined directly by the rates R_n , while the parameters β_n , which are generally chosen to increase monotonically¹⁵, have the effect of determining the film roughness. As with our model above, we find that additional variation in the values of β_n for the first few layers is required to obtain a good fit to data. We define β_1 and β_2 as free parameters, while for layers $n \geq 3$, $\beta = \beta_3(n - 2)^\alpha$. Because of the explicit time dependence of the intermediate functions J_n , this model does not strictly allow for a coverage dependent growth rate. Nevertheless, allowing different values for R_n does approximate such

behavior. Just as with the Cohen model, for systems exhibiting growth rate acceleration, the values of R_1 are chosen to differ from that of $R_{n>1}$. To calculate the t_n 's, we make the explicit assumption that layer N is completed at time $t_N = 1/R_1 + \sum_{n=2}^N 1/R_{n>1}$, leading to $t_n = nR_{n>1}/(R_1 R_{n>1})$. Thus, this model includes six parameters, R_1 , $R_{n>1}$, β_1 , β_2 , β_3 , and α .

The last model employed for our comparison is a simplified version of an atomistic, rate-equation model developed by Trofimov et al.^{39–43}. Unlike the layer-wise models just described, this model includes three rate equations for each layer, describing the rates of change of the adatom density, island density, and coverage. Downhill transport is controlled by a so-called “feeding zone” ξ_n of each layer n : atoms that are incident onto the feeding zone ξ_n of layer n remain on that layer and hence contribute to layer $n + 1$. Adatoms that land on top of layer n but outside this feeding zone diffuse downward, thus increasing θ_n . A clear advantage of the Trofimov model is the ability to directly connect morphology, including in-plane parameters such as the nucleation density, evolves as a function of layer number, and as a function of real, physical parameters such as D/J , the ratio of adatom diffusivity to the incident flux. For example, it is found that, even for homoepitaxy, the saturation island density decreases as a function of layer number during LBL growth⁴¹. This phenomena has recently been directly observed in SrTiO₃ homoepitaxy using pulsed laser deposition⁴⁸.

For the limited problem of examining layer coverages, the Trofimov model may be re-parameterized so that it, like the models described above, includes only one equation per layer. Examination of Ref. [41] shows that all of the atomistic physics is contained in the evaluation of the critical coverage for each layer $\theta_{n,\text{cr}}$. Defining this as a fit parameter, we have:

$$\frac{d\theta_n}{dt} = \begin{cases} R_1(1 - \theta_1) + R_{n>1}(\theta_1 - \xi_1) , & n = 1 \\ R_{n>1}(\xi_{n-1} - \xi_n) , & n > 1, \end{cases} \quad (14)$$

where

$$\xi_n = \begin{cases} 0 , & \theta_n < \theta_{n,\text{cr}} \\ 1 - \exp\left(-\left[\sqrt{-\ln(1 - \theta_n)} - \sqrt{-\ln(1 - \theta_{n,\text{cr}})}\right]^2\right) , & \theta_n \geq \theta_{n,\text{cr}}. \end{cases} \quad (15)$$

As in the models above, we have incorporated variation in the sticking coefficient of incident species through the parameters R_1 and $R_{n>1}$, and obtain reasonable fits by allowing $\theta_{n,\text{cr}}$ to change with layer number. The analysis shown below incorporates six growth parameters,

R_1 , $R_{n>1}$, $\theta_{1,\text{cr}}$, $\theta_{2,\text{cr}}$, $\theta_{\infty,\text{cr}}$, and a parameter N_0 determining the asymptotic approach to $\theta_{\infty,\text{cr}}$.

IV. COMPARISON TO EXPERIMENT

A. Pentacene/SiO₂

Before discussing analysis of the X-ray data shown in Fig. 1a, we note that the AFM results in Fig. 1B-E obtained by hyperthermal growth are consistent with those of prior, voluminous work on (thermal) pentacene/SiO₂ MBE^{25–27,45,49}. Growth begins in a LBL mode, so that the first layer is nearly complete before the second layer nucleates. Subsequently, roughness increases quickly, resulting in a late-time morphology characterized by large, multilayer islands. The precise nature of this transition varies with growth conditions—particularly temperature²⁷.

Figure 4A reproduces the data from the thickest film shown in Fig. 1, along with fits to the three models described in section IIIB. Figure 4B-C show the evolution of layer coverages and rms roughness, respectively, resulting from the fits in Fig. 4A, in addition to the rms roughness values (4C) obtained from AFM on each of the four films. As expected from the agreement in Fig. 4A, reasonably good agreement is also obtained in rms roughness evolution among the models and the AFM results, through a thickness of 2.5 ML. Beyond this thickness, clear discrepancies are observed.

The fit parameters are shown in Table I. Since deposition was performed directly on clean SiO₂, as confirmed by x-ray reflectivity prior to growth, no interfacial layer was included ($\rho_1 = 0$, $\tau = 0$). For ρ_0 , a bulk mass density of 2.2 g/cm³ was used, corresponding to the assumption that electron density is proportional to mass density. For this case, no growth rate acceleration is observed: allowing $R_{n>1}$ to vary from R_1 does not improve the fit. Thus, $R_{n>1} = R_1$ for the fits shown. All models reproduce the conspicuous features of the data, giving R-squared values of 99.4% or higher. However, the fits are not perfect: the Braun/Kaganer and Trofimov models give comparable quality fits, with χ^2 values of 35 and 34, respectively, indicating that the differences between the model and data are statistically significant⁵⁰. For the modified Cohen model, the best fit, with $\chi^2 = 7$, was obtained with ΔE_2 and $\theta_{\infty,\text{cr}}$ at 0, and the remaining parameters as shown in Table I.

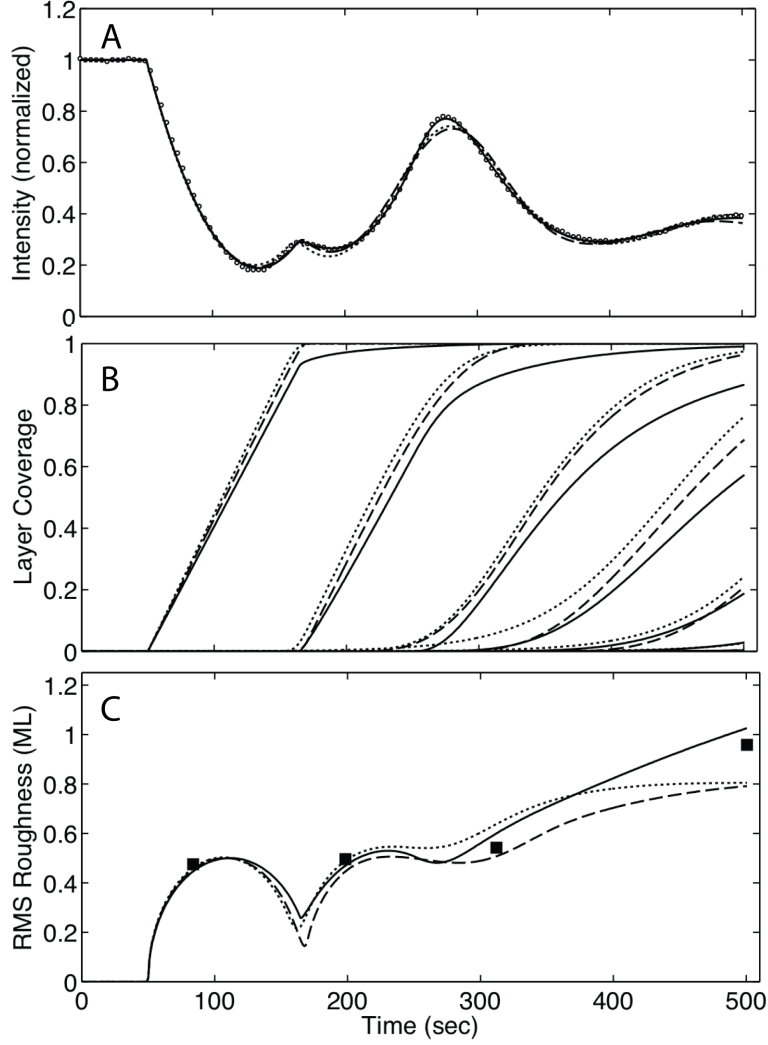


FIG. 4: a) (open circles) X-ray reflectivity data obtained near the pentacene anti-Bragg position during pentacene deposition on SiO_2 . Also shown are best-fit curves from three models described in the text, the modified Cohen model (solid line), the Braun/Kaganer model (dashed line), and the modified Trofimov model (dotted line). b) Layer coverages from the three models shown in (a). b) Lines show the evolution of root-mean square roughness obtained from the three models shown in (a) and (b). Filled squares are measured rms roughness values obtained from ex situ AFM.

The fact that the χ^2 values differ significantly from 1 reflects, in part, the high accuracy of the data: the average intensity \bar{I} in Fig. 4a is 2.4×10^4 , so that the mean statistical uncertainty in the data $\langle \sqrt{I}/I \rangle$ is 0.7%. Alternatively, we compare the mean absolute residual with the mean of the data $\langle |I - I_m|/I_m \rangle$. For the fits in Fig. 4, the Cohen model differs from the data by 1.4%, the Braun/Kaganer and Trofimov models by 3.2%.

Cohen		Braun		Trofimov	
ρ_2	1.458 ± 0.005	ρ_2	1.354 ± 0.006	ρ_2	1.373 ± 0.005
Δ	0.202 ± 0.001	Δ	0.172 ± 0.001	Δ	0.1913 ± 0.001
L	0.4579 ± 0.0006	L	0.482 ± 0.001	L	0.467 ± 0.001
R_1	$0.0081 \pm 3e^{-5}$	R_1	$0.0089 \pm 1e^{-5}$	R_1	$0.0086 \pm 1e^{-5}$
δ	0.88 ± 0.01				
E_1	-0.55 ± 0.03	β_1	5.8 ± 1.7	$\theta_{1,\text{cr}}$	0.88 ± 0.05
$\theta_{1,\text{cr}}$	0.93 ± 0.01				
$\theta_{2,\text{cr}}$	0.65 ± 0.01	β_2	38.8 ± 0.5	$\theta_{2,\text{cr}}$	0.341 ± 0.004
ΔE_N	0.99 ± 0.03	β_3	87.0 ± 0.5	$\theta_{\infty,\text{cr}}$	0.078 ± 0.001
N_0	0.01 ± 0.003	α	0.0 ± 0.01	N_0	0.07

TABLE I: Fit parameters for the three fits shown in Fig. 4

In view of the greater number of parameters in the modified Cohen model, the better fit is not unexpected. The question remains whether this statistically improved fit corresponds to more accurate layer coverages in Fig. 4B. The rms roughnesses appear to suggest that this is the case, since the measured rms roughness at $t = 500\text{s}$ corresponds more closely to the modified Cohen model than to the others. A more detailed comparison of the models and films is given in Fig. 5 which shows height distributions obtained by the AFM data in Fig. 1 as well as the height distributions obtained from each of the best-fit simulations in Fig. 4. In each plot, discrete height distributions (represented as black bars) were obtained by fitting the continuous distribution to a sum of several Gaussian peaks, one per layer, and equating the area of each peak to fractional, exposed occupancies for each layer c_n . If the c_n 's are normalized such that $\sum_n c_n = 1$, they are related to the layer coverages θ_n as: $c_n = \theta_n - \theta_{n+1}$. For AFM images, the indexing n of layers is chosen such that the total thickness $\tau = \sum_n n c_n = \sum_n \theta_n$ most closely matches thickness estimates provided either by the x-ray data or, alternatively, by the sub-monolayer growth rate. Figure 5 reveals that the agreement between the modified Cohen model (dark gray) and AFM is not conspicuously better, and may in fact be worse than that of the other simulations. Thus, the lower value of χ^2 does not necessarily imply a more accurate representation of the true morphological evolution of the film.

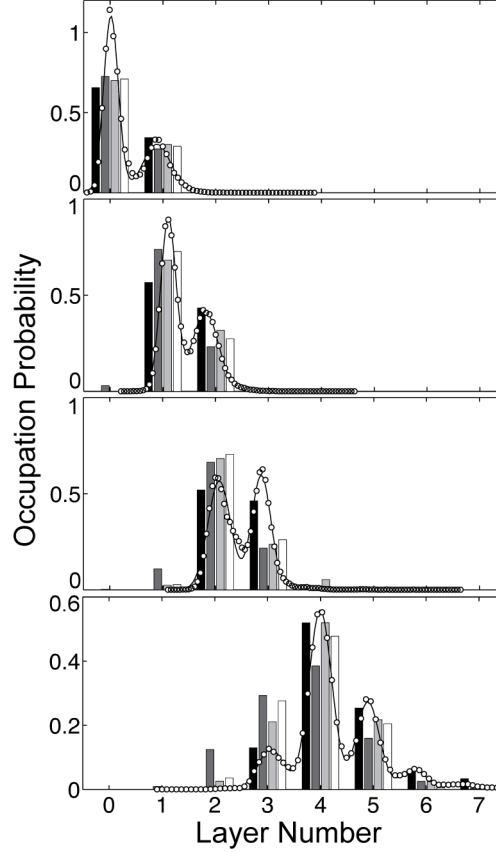


FIG. 5: Height distributions obtained from the AFM images in Fig. 1 and from best-fit simulations shown in Fig. 4A. Open circles represent height distributions obtained directly from the AFM data, solid lines indicate fits of these data with a sum of several Gaussian distributions (one per layer), and black bars indicate the area of each Gaussian distribution so obtained. Dark grey, light gray, and white bars represent height distributions obtained from the Cohen, Braun/Kaganer, and Trofimov models, respectively.

The parameters in Table I warrant several comments. First, the values of ρ_2 for all three fits are close to, but somewhat larger than that of bulk pentacene, 1.3 g/cm^3 . The sign of this discrepancy is consistent with the expected error due to the uniform slab approximation. The fact that the electron density in pentacene is slightly concentrated around the molecular center (along the c axis) has the effect, at L values below the first Bragg Peak, of increasing the scattering amplitude of this layer compared to a uniform slab with equivalent average density. A larger, *uniform* electron density compensates for this difference. Second, although the data are nominally obtained at $L = 0.5$ (the anti-Bragg position), good fits require $L \approx 0.46 - 0.48$, and an offset between the substrate and the first layer of $\Delta_z = \Delta \times c \approx 3\text{\AA}$.

Possible contributions to the deviation of L from 0.5 include the experimental uncertainty, defined by the detector slits to be $\Delta L = 0.03$, and a change, with layer thickness, of the pentacene d-spacing c . Such a change has been reported by Fritz et al.⁵¹. The offset Δ_z is assumed to correspond to a thin interfacial region at the SiO_2/film interface. The remaining parameters in Table I, those describing the growth morphology, all show effectively the same, monotonic trend from smooth to rough growth. Specifically, rougher growth corresponds to increasing values of β_n in the Braun model, decreasing values of $\theta_{n,\text{cr}}$ in the Trofimov model, and a combination of increasing E_n and decreasing $\theta_{n,\text{cr}}$ in the modified Cohen model.

Finally, we note that the three models predict growth rates R_1 which vary from 0.0081 to 0.0089 ML/second. Evidently, even for the fairly straightforward problem of determining the growth rate of this simple system, the details of the model strongly affect the results. The origin of this variation is the link between the the onset of roughness and the appearance of a peak. In general, extrema in the scattering data occur when the growth rate of one layer overtakes that of the layer below it. For perfect LBL growth, this moment coincides with layer completion, producing cusp-like peaks. But for a film undergoing roughening, this transition can occur at lower coverage for each consecutive layer, resulting in a shorter time between peaks than the time to deposit 1 ML. If the roughening transition is abrupt, the growth rate can appear to accelerate. This is well illustrated by Fig. 4A. Growth begins at $t = 50\text{s}$, and the first two local maxima occur at $t = 167\text{s}$ and $t = 275\text{s}$, corresponding to growth rate estimates of 0.0085 and 0.0093 ML/second. The three different models represented in Fig. 4A model the onset of roughness in slightly different ways, resulting in three different estimates of growth rate.

The variation in best-fit growth rates among different models, all of which fit the data well, raises the question of whether there is an independent means of measuring growth rate and, especially, of determining whether or not growth rate acceleration has occurred. We reiterate that for the hyperthermal growth method used here^{20,23}, the use of a quartz crystal monitor is not possible due both to the narrowly-directed beam profile and the possibility that sticking coefficients are generally substrate-dependent. We present two alternatives. First, the cusp-like nature of the first local maximum in Fig. 4A suggests that this peak closely coincides with completion of the first layer. Thus, *provided* that we are confident that growth rate acceleration does not occur, and that the surface morphology does not develop large height asymmetries during the first layer²¹, the growth rate estimate given by

the peak, 0.0085 ML/second should provide an accurate estimate of the growth rate. This growth rate falls within the results from the three fits.

A second alternative measure of the growth rate can be made using the height distributions represented in Fig. 5 to obtain a plot of thickness vs. time. As noted above, the thickness is obtained as the center-of-mass of the height distributions, under the assumption that the layers are properly indexed. The circles in Figure 6 represent the thicknesses of the four films in Fig. 1 obtained in this manner, along with the best-fit line to those data. Clearly, a line describes the data well. Unfortunately, the growth rate obtained in this fashion, 0.0096 ± 0.0002 ML/s, does not fall within the growth rates obtained from fits, and is not consistent with 0.0085 ML/s obtained by simple inspection of Fig. 4A. In fact, it is difficult to reconcile the x-ray data with a growth rate of 0.0096 ML/s, since this growth rate would imply that the sharp, cusp-like peak at $t = 167$ s occurs at a thickness *greater* than 1 ML. We account for this difference by noting that the AFM measurements were performed ≈ 1.5 mm away from where the x-ray measurements were performed on the film⁵⁴. It is plausible that there could be a 10% difference in growth rate between these locations. We also note that AFM tip artifacts will always result in an *overestimate* of the film thickness, since holes will appear smaller than they actually are, while islands will appear larger than the actually are.

Regardless of the disagreement in growth rate implied by the x-ray and AFM analysis, the two approaches agree with regard to the absence of growth rate acceleration. Referring again to Fig. 6, this conclusion comes from the fact that the best-fit line of the pentacene data intersects the origin to within 0.02 ML. This finding contrasts the case of DIP/SiO₂, also represented in Fig. 6 and discussed in detail below.

B. DIP/SiO₂

Figure 7 shows AFM data obtained from a thickness series of DIP/SiO₂. As in Fig. 1, these films were grown in immediate succession on the same substrate. In contrast to the films in Fig. 1 which were grown at 40°C, the films in Fig. 7 were grown at a substrate temperature of 89°C. This increased temperature may contribute to the two most conspicuous differences between Figs. 7 and 1: DIP exhibits a compact island morphology and more persistent LBL growth.

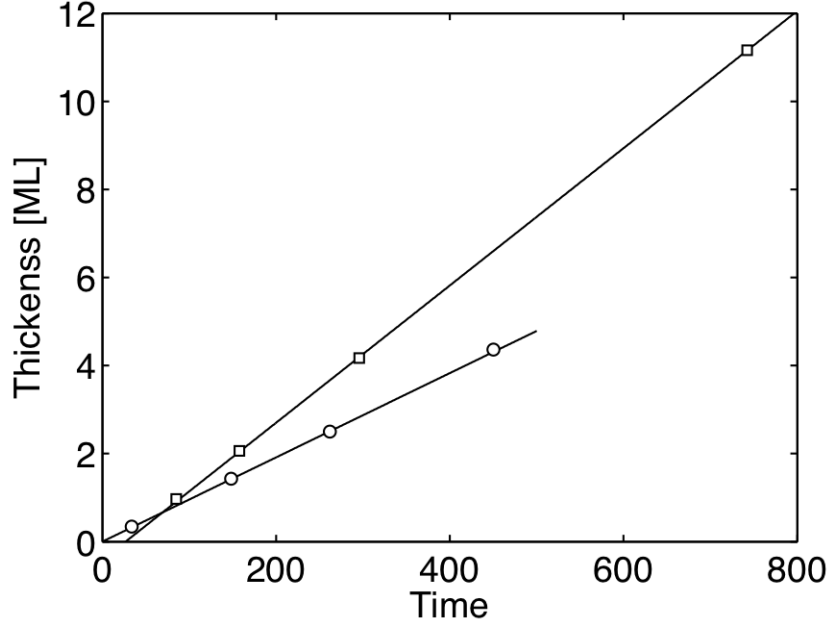


FIG. 6: Thickness, determined by AFM as described in the text, vs. time of (circles) pentacene films represented in Fig. 1 and (squares) DIP films represented in Fig. 7. Also shown are linear fits to the AFM-determined thicknesses, as described in the text. The best-fit line to the pentacene data intersects the origin, indicating an absence of growth rate acceleration, and a growth rate of 0.0096 ± 0.0002 ML/s. For DIP, only the later three point are used for the fit, yielding a line that does not intersect the origin, (indicating the presence of growth rate acceleration) and that gives a late-time growth rate $R_{n>1}$ of 0.0156 ± 0.001 ML/s.

The squares in Figure 6 represent thickness vs. time of the four films in Fig. 7, obtained by combining data in Fig. 7 with qualitative analysis of in situ x-ray data acquired during growth. In contrast to the pentacene case, a best-fit line to these four points clearly has a negative intercept, indicating growth rate acceleration. Because of this, only the later three points are used for the fit in Fig. 6, yielding a late-time growth rate of 0.0156 ± 0.001 ML/s. To measure of the degree of acceleration, we turn to quantitative analysis.

Figure 8 shows (A) x-ray data obtained from the thickest of the films in Fig. 7, along with fits to these data, (B) resulting layer coverages and (C) rms roughness evolution for the same three models as in Fig. 4. Fig. 8C also shows rms roughnesses obtained from the AFM data in Fig. 7. In general, the modeled x-ray intensities in Fig. 8A show reasonable, but noticeably worse agreement than in Fig. 4A, and yield correspondingly worse χ^2 values of 445, 756, and 509 for the Cohen, Braun/Kaganer, and Trofimov models, respectively. As

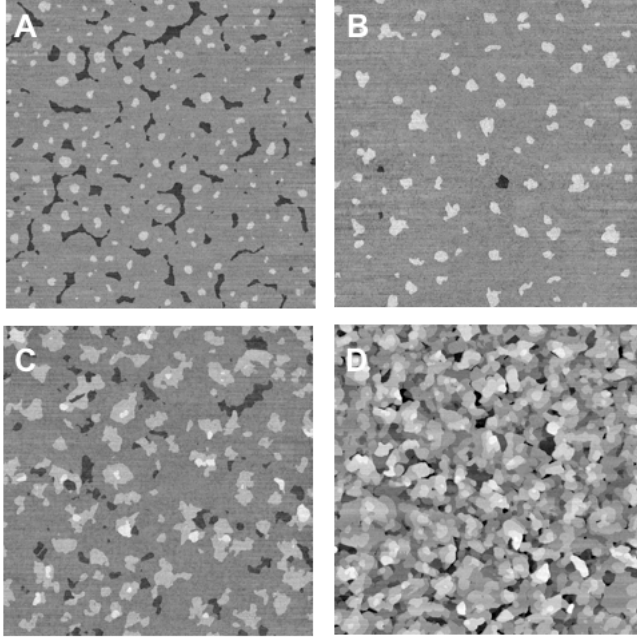


FIG. 7: AFM images of four thin films of DIP/SiO₂ of increasing thickness grown in immediate succession on four areas of the same substrate: (A) 0.97 ML; (B) 2.06 ML; (C) 4.17 ML; (D) 11.16 ML. All images are 20 μ m \times 20 μ m

with the fits in Fig. 4A, we also compare the mean residual to the mean value of the data $\langle |I - I_m| / I \rangle$, obtaining values of 9.2%, 12%, and 10%. The reasons for the difference in fit quality between Figs. 4A and 8A are unclear. However, previous work on DIP/SiO₂⁵² has demonstrated a clear structural change in a DIP thin film during growth of the first five layers. Such a change would have the effect of making some of the x-ray parameters discussed in section III A time-dependent.

Referring to Fig. 8C, all three models compare very well with the AFM data up to $t = 400$ s, corresponding to a thickness of 4 ML, beyond which the models diverge both from each other and from the actual film. At $t = 800$ s, corresponding to a thickness of 11.2 ML, the Cohen and Braun/Kaganer overestimate the roughness, whereas the Trofimov model underestimates it. These observations are reflected in more detail in Fig. 9, which compares the actual height distributions obtained both from the AFM data and from the models. The correspondence between the simulated and measured height distributions for the three thinner films is very good, whereas all three simulations depart significantly from the measured height distribution of the thickest film in the series.

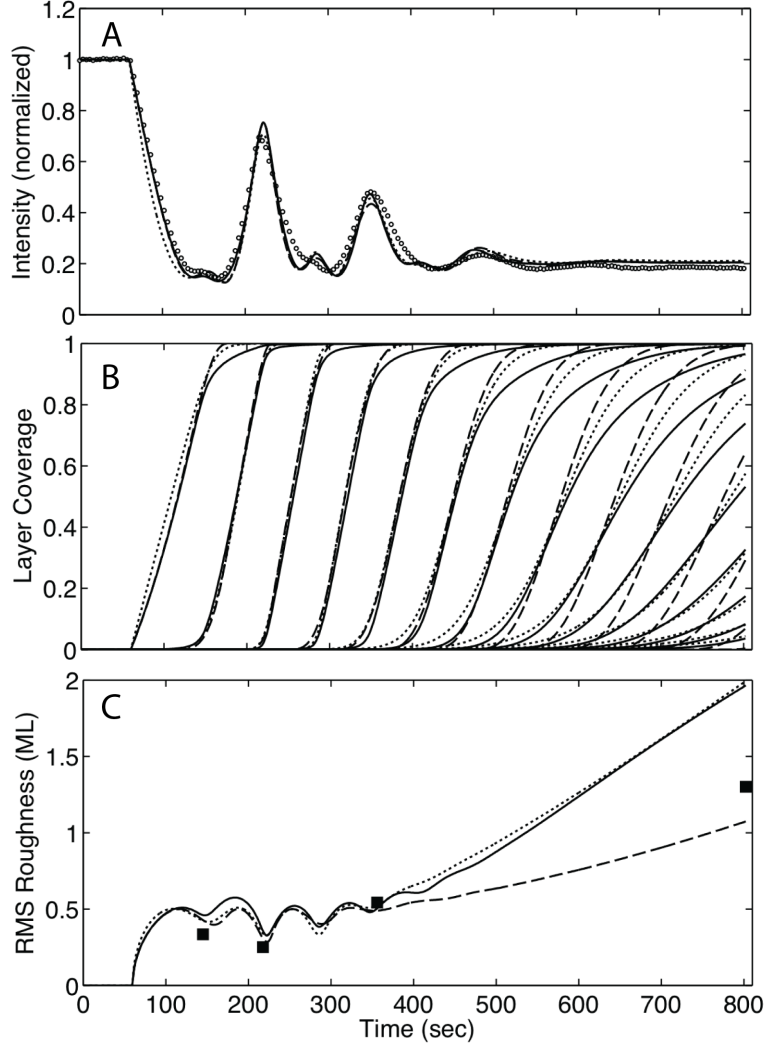


FIG. 8: a) (open circles) X-ray reflectivity data obtained near the DIP anti-Bragg position during DIP deposition on SiO_2 . Also shown are best-fit curves from three models described in the text, the modified Cohen model (solid line), the Braun/Kaganer model (dashed line), and the modified Trofimov model (dotted line). b) Layer coverages from the three models shown in (a). b) Lines show the evolution of root-mean square roughness obtained from the three models shown in (a) and (b). Filled squares are measured rms roughness values obtained from ex situ AFM.

Echoing the analysis of pentacene/ SiO_2 , the Cohen model, which has the lowest value of χ^2 compared to the other two models, nevertheless does not provide a conspicuously better representation of film growth. In fact, both the Cohen and Braun/Kaganer models tended towards second, deeper χ^2 minima ($\chi^2 = 285, 417$, respectively) characterized by the disappearance of the shallow local maximum near $t = 150\text{s}$. The film morphology implied

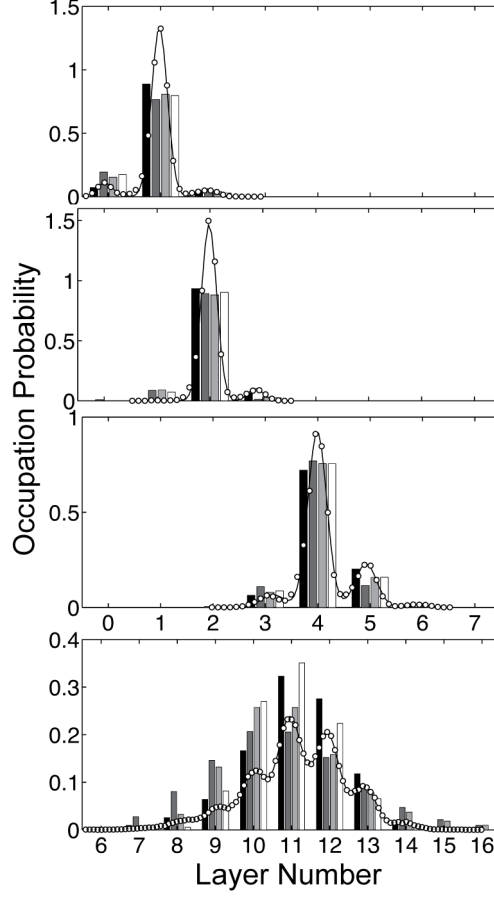


FIG. 9: Height distributions obtained from the AFM images in Fig. 7 and from best-fit simulations shown in Fig. 8A. Open circles represent height distributions obtained directly from the AFM data, solid lines indicate fits of these data with a sum of several Gaussian distributions (one per layer), and black bars indicate the area of each Gaussian distribution so obtained. Dark grey, light gray, and white bars represent height distributions obtained from the Cohen, Braun/Kaganer, and Trofimov models, respectively.

by these alternative fits are inconsistent with the AFM data (see Appendix C, Fig. 10). To avoid these minima, only a subset of parameters could be allowed to vary simultaneously, taking care that the best-fit model reproduced, at least weakly, each of the extrema in the data.

The parameters for the fits in Fig. 8A are shown in Table II. As for the analysis of Fig. 4A, these fits presupposed the absence of an interfacial layer ($\rho_1 = 0$, $\tau = 0$), and employed $\rho_0 = 2.2\text{g/cm}^3$. For the Cohen model, $\theta_{1,\text{cr}}$, $\theta_{2,\text{cr}}$, and $\theta_{\infty,\text{cr}}$ were all fixed at 0.

An interesting feature of Fig. 8C, in both the AFM data and the models, is that the rms

Cohen		Braun		Trofimov	
ρ_2	1.43 ± 0.01	ρ_2	1.40 ± 0.01	ρ_2	1.425 ± 0.01
Δ	-0.116 ± 0.001	Δ	-0.115 ± 0.002	Δ	-0.116 ± 0.002
L	0.488 ± 0.001	L	0.488 ± 0.001	L	0.488 ± 0.001
R_1	$0.0069 \pm 8e^{-5}$	R_1	$0.0103 \pm 6e^{-5}$	R_1	$0.0069 \pm 8e^{-5}$
$R_{n>1}$	0.0151 ± 0.0001	$R_{n>1}$	0.0156 ± 0.0001	$R_{n>1}$	0.0153 ± 0.0001
δ	0.935 ± 0.004	β_1	20	$\theta_{1,\text{cr}}$	0.49 ± 0.04
E_1	-1.9	β_2	9.9 ± 1	$\theta_{2,\text{cr}}$	0.66 ± 0.02
ΔE_2	-1.29 ± 0.09	β_3	10.2 ± 0.7	$\theta_{\infty,\text{cr}}$	0.0
ΔE_N	8.7 ± 0.4	α	1.13 ± 0.07	N_0	2.86 ± 0.1
N_0	10 ± 0.2				

TABLE II: Fit parameters for the three fits shown in Fig. 8

roughness at film thickness $\tau = 2$ is *smaller* than that at $\tau = 1$. This is reflected in the fact (see Table II) that the parameters controlling interlayer transport for all three models do not change monotonically, as in Table I. The causes of this behavior are outside the scope of this paper: however we observe that it could be related either to the structural evolution of the DIP film⁵² or to the dependence of growth rate on coverage.

The key difference between Tables II and I is the appearance of the additional parameter, $R_{n>1}$, corresponding to the late-time growth rate of the film. Above, we found that the AFM data in Fig. 6 gave a late-time growth rate of 0.0156 ML/s. Referring to Tab. II, we find that this late-time growth rate agrees well with that obtained from all three models. On the other hand, the Cohen and Trofimov models give growth rate accelerations, $(R_{n>1} - R_1)/R_1$, of 112% and 122%, respectively. The Braun/Kaganer model, which we reiterate is not expected to model growth rate acceleration accurately, gives a more modest growth rate acceleration of 56%.

To corroborate the growth rate acceleration obtained from the model, we observe that, for the case of perfect LBL growth, the degree of growth rate acceleration may be estimated from a plot of thickness vs. time, as in Fig. 6. In this case, both the Cohen and Trofimov

models describe the growth of the first layer as

$$\frac{d\theta_1}{dt} = R_1(1 - \theta_1) + R_{n>1}\theta_1, \quad (16)$$

and the remaining layers as

$$\frac{d\theta_n}{dt} = R_{n>1}(1 - \theta_n). \quad (17)$$

Solving this system yields the total thickness $\tau = \sum_n \theta_n$ as a function of time:

$$\tau(t) = \begin{cases} \frac{R_1}{R_{n>1}-R_1} (e^{(R_{n>1}-R_1)t} - 1) & , t \leq t_1 \\ 1 + R_{n>1}(t - t_1) & , t > t_1, \end{cases} \quad (18)$$

where $t_1 = \log((R_{n>1} - R_1)/(R_1 + 1))/(R_{n>1} - R_1)$. We now identify the linear regime in Eq. 18 with the best-fit line to the late-time thickness data in Fig. 6. Setting the intercept b of that line equal to $1 - R_{n>1}t_1$ yields

$$(1 - b) \left(\frac{R_1}{R_{n>1}} - 1 \right) = \log \left(\frac{R_1}{R_{n>1}} \right), \quad (19)$$

which can be numerically solved for R_1 . For the DIP data in Fig. 6, $R_{n>1} = 0.0156$ ML/s and $b = -0.417$ ML, which give the result $R_1 = 0.0074$ ML/s. This corresponds to a growth rate acceleration of 111%, in good agreement with the values from the Cohen and Trofimov models described above. We conclude that, at least for systems exhibiting relatively smooth growth at early times, these models provide an accurate means of determining growth rate acceleration.

V. SUMMARY AND CONCLUSIONS

In this paper, we have provided the first comparative study of the problem of obtaining surface morphology from in situ, time resolved XRR data. We described three mean-field models of thin film growth, along with detailed examples of their application to quantitative analysis of XRR data obtained at the anti-Bragg position during growth. Two sets of organic thin films were grown using hyperthermal deposition, pentacene/SiO₂ and DIP/SiO₂. For each system, in situ XRR data was obtained during growth of four films, grown to different thicknesses, under nominally identical conditions. The XRR data were fit to each of the three models, resulting in detailed simulations of the time-dependent morphology of each

film. Finally, these simulated morphologies were directly compared with AFM data from each of the four films to critically evaluate the quality of each simulation.

We find, first, that all of the models provide reasonable descriptions of both the XRR data and, at early times, the surface morphology of an evolving film. Second, we show that better, statistical fits to the data do not necessarily imply more faithful reproduction of the true surface morphology. In the case of pentacene/SiO₂, which exhibits an abrupt roughening transition near 2 ML, different models obtain values for the total growth rate that vary by as much as 10%. For DIP/SiO₂, which exhibit extended LBL oscillations, we find that fits of XRR data to the modified Cohen and Trofimov models both correctly extract the degree of growth rate acceleration.

A key feature of the modified Cohen and Trofimov models is that they both incorporate measurable quantities, such as the layer step-edge density and the critical coverage for next-layer nucleation, as fit parameters. Future work will aim to test whether these parameters, rather than only the layer coverages, can be extracted from XRR data during growth. For example, we will investigate how accurately the critical coverage parameter, θ_{cr} extracted from fits of XRR data to the Trofimov model, corresponds to independent measurements of θ_{cr} . We believe that such work will contribute significantly to the technologically important challenge of understanding, and ultimately controlling, physical and experimental factors determining surface morphology in thin films.

Appendix A: Thin Film Scattering Amplitudes Parameterized for In Situ XRR

Here, we derive Eq. 2 from Eq. 1, resulting in approximate values of $A_{\text{film}}/A_{\text{sub}}$ and ϕ_{sub} for the technologically relevant case of an organic thin film on a substrate with a thin interfacial layer. Referring to Figure 2, we begin by dividing the integral in Eq. 1 into separate volumes, treating the buried substrate, the interfacial layer, and each crystalline layer of the film as distinct. Since we are only interested in the specular intensity, we ignore the fact that the film layers are only partially complete, and instead treat the coverage θ_n as a modification to the density ρ_2 . This step ignores the q_{\parallel} contribution of the diffuse scattering^{48,53}, which depends on both details of the system as well as instrumental resolution. Neglecting the

(static) roughness of each interface, and allowing only θ_1 to be nonzero, Eq. 1 becomes

$$A(q_z)/A_0 = \rho_0 \int_{-\infty}^{-T_1} dz e^{-iq_z z} + \rho_1 \int_{-T_1}^0 dz e^{-iq_z z} + \theta_1 \int_0^c dz \rho_2(z) e^{-iq_z z}. \quad (\text{A1})$$

We next carry out the integrals, while at the same time including a term, Δ_z corresponding to a height correction of the first layer:

$$A(q_z)/A_0 = \frac{i}{q_z} [\rho_1 + (\rho_0 - \rho_1)e^{iq_z T_1}] + A_{\text{mol}}(q_z) e^{-iq_z(c/2+\Delta_z)} \sum_{n=1}^N \theta_n e^{-i(n-1)q_z c}. \quad (\text{A2})$$

The term $A_{\text{mol}}(q_z)$ is the molecular structure factor, defined as

$$A_{\text{mol}}(q_z) = \sum_m e^{-iq_z \tau_m} \int dz \rho_m(z) e^{-iq_z z}, \quad (\text{A3})$$

where the sum is over atoms in a unit cell, and τ_m is the height of each atom relative to the center of the molecule (defined as $z = c/2$) above the substrate, and $\rho_m(z)$ is the linearly-projected electron density of atom m . Finally, we factor out the phasor in front of the right-hand summation, and convert to reciprocal lattice units $L = q_z/(2\pi/c)$, defining $\tau = T_1/c$, $\Delta = \Delta_z/c$. Equation A2 then becomes

$$A(q_z)/A_0 = \left[\frac{2\pi}{cL} i e^{i\pi L(1+2\Delta)} (\rho_1 + (\rho_0 - \rho_1)e^{i2\pi L\tau}) + A_{\text{mol}}(q_z) \sum_{n=1}^N \theta_n e^{-i(n-1)2\pi L} \right] \quad (\text{A4})$$

Equation A4 accomplishes the goal of providing an explicit formula for the parameters ϕ_{sub} and $A_{\text{film}}/A_{\text{sub}}$ in Equation 2 in terms of physical parameters of the film. We note too, that for centrosymmetric molecules such as pentacene, A_{mol} is pure real, so that at the anti-Bragg position ($L = 0.5$), the second term contributes only pure real terms to the complex sum.

For large, organic molecules, the antiBragg position probes density fluctuations on an approximate length scale $l = 2\pi/q_z = c/L$, which is large compared to interatomic distances. As a result, a molecular layer is well approximated by a uniform density slab. In this approximation, A_{mol} can be written

$$A_{\text{mol}}(q_z) = 2\rho_2 \left(\frac{2\pi}{c} \right) \frac{\sin(\pi L)}{L}. \quad (\text{A5})$$

We note that the simple case of homoepitaxy can be recovered by setting the densities equal and $\tau = 0$. The uniform slab approximation at the anti-Bragg position $L = 0.5$ then gives the familiar result¹⁸:

$$I_{\text{AB}} \propto |A_{\text{AB}}|^2 = \left| 1 - 2 * \sum_{n=1}^N \theta_n (-1)^{n-1} \right|^2 \quad (\text{A6})$$

Appendix B: Scattering Amplitude evolution during LBL and SF growth on vicinal surfaces.

To compare trajectories of the total scattering amplitude during LBL and SF growth, we imagine an ideal, vicinal substrate with step-height c and terrace width W , and with the positive x direction perpendicular to, and pointing towards uphill steps. We choose the origin to coincide with the center of a terrace in x and height z of the first growing layer. The scattering amplitude A_{vic} of a film with a total of N_L partially complete layers (compare with Eq. 2) is then

$$A_{\text{vic}} = \sum_{k=-N_W}^{N_W} e^{-i(q_z c + q_x W)k} \left[A_{\text{sub}} e^{i\phi_{\text{sub}}} + \sum_{n=1}^{N_L} e^{-iq_z c(n-1)} A_{\text{ter}}(\theta_n) \right] \quad (\text{B1})$$

where $A_{\text{ter},n}(\theta_n)$ is the scattering amplitude of layer n with fractional coverage θ_n . The left-hand sum in Eq. B1 is over $N_T = 2N_W + 1$ terraces, and defines the specular condition as $q_z c = -q_x W$. In perfect SF growth, each layer n commences only when layer $n - 1$ is complete, and grows from the up-hill step at $x = W/2$, advancing from right to left until reaching the down-hill step at $x = -W/2$ at $\theta_n = 1$. Thus,

$$A_{\text{ter,SF}}(\theta_n) = f \int_{W/2-\theta W}^{W/2} dx e^{-iq_x x}, \quad (\text{B2})$$

where f is the electron density per unit length of the growing layer. Along the specular rod, we can substitute $-q_z c$ with $q_x W$ in all of the terms $e^{-iq_z c(n-1)}$ in Eq. B1. Next we can bring these prefactors into the integrands and substitute variables, so that the right-hand term in brackets becomes

$$\sum_{n=1}^{N_L} e^{-iq_z c(n-1)} A_{\text{ter}}(\theta_n) = f \left[\int_{-W/2}^{W/2} dx e^{-iq_x x} + \int_{-3W/2}^{-W/2} dx e^{-iq_x x} \dots + \int_{W/2-(N_L-1)W}^{W/2-(N_L-1+\theta_{N_L})W} dx e^{-iq_x x} \right], \quad (\text{B3})$$

All of the integrals in Eq. B2 may now be combined. Identifying the film thickness $\tau = N_L - 1 + \theta_{N_L}$, we have

$$\sum_{n=1}^{N_L} e^{-iq_z c(n-1)} A_{\text{ter},n}(\theta) = f \int_{W/2-W\tau}^{W/2} dx e^{-iq_x x} = \frac{f}{iq_x} e^{-iq_x W/2} [e^{iq_x W\tau} - 1]. \quad (\text{B4})$$

for the total film scattering amplitude along the specular rod. Eq. B4 shows that the scattering amplitude in SF growth completes a circle in the complex plane whenever $q_x W\tau = 2\pi n$, or equivalently (recalling $-q_x W = q_z c = 2\pi L$), whenever $\tau = n/L$.

In LBL growth, deposited material lands randomly on each terrace, so the scattering amplitude of a partially filled layer is just Eq.B2 *evaluated* at $\theta = 1$, then multiplied by the actual coverage θ_n :

$$A_{\text{ter,LBL}}(\theta_n) = \theta_n 2f \frac{\sin(q_x W/2)}{q_x}. \quad (\text{B5})$$

Just like Eq. 2, Eq. B1 with the substitution of Eq. B5 results in regular, polygonal trajectories in the total scattering amplitude. The effect of considering a vicinal, rather than singular substrate, is to reduce the effective electron density of a layer. For example, at the anti-Bragg position, Eq. B5 gives $A_{\text{ter,LBL}}(\theta_n) = f\theta_n W$ for a singular surface ($q_x = 0$), but $A_{\text{ter,LBL}}(\theta_n) = (2/\pi)f\theta_n W$ for a vicinal surface ($q_x W = \pi$).

In homoepitaxy, the circular trajectory in Eq. B4 for the scattering amplitude in the specular condition must result in constant intensity. In that case, and making use of Eq. B5, the term $A_{\text{sub}}e^{i\phi_{\text{sub}}}$ is evaluated as :

$$\begin{aligned} A_{\text{sub}}e^{i\phi_{\text{sub}}} &= A_{\text{ter}} \sum_{n=1}^{\infty} e^{iq_z cn - \epsilon n} \\ &= A_{\text{ter}} \frac{e^{iq_z c}}{1 - e^{iq_z c}} \\ &= 2f \frac{\sin(q_x W/2)}{q_x} \frac{e^{iq_z c/2}}{-2i \sin(q_z c/2)} \\ &= \frac{f}{iq_x} e^{-iq_x W/2}, \end{aligned} \quad (\text{B6})$$

where A_{ter} is Eq. B5 evaluated at $\theta_n = 1$, and we have again used $q_z c = -q_x W$. Clearly, adding Eq. B6 to Eq. B4 translates the circle to the origin, so that the scattered intensity is constant with increasing τ .

Appendix C: Additional Fits to in situ XRR data during DIP/SiO₂ Growth

Figure 10 shows alternate fits to the same data represented by Fig.8 using the modified Cohen and Braun/Kaganer models described in the text.

Acknowledgments

This work was supported by the Cornell Center for Materials Research, a National Science Foundation Materials Research Science and Engineering Center (NSF-DMR-0520404), and

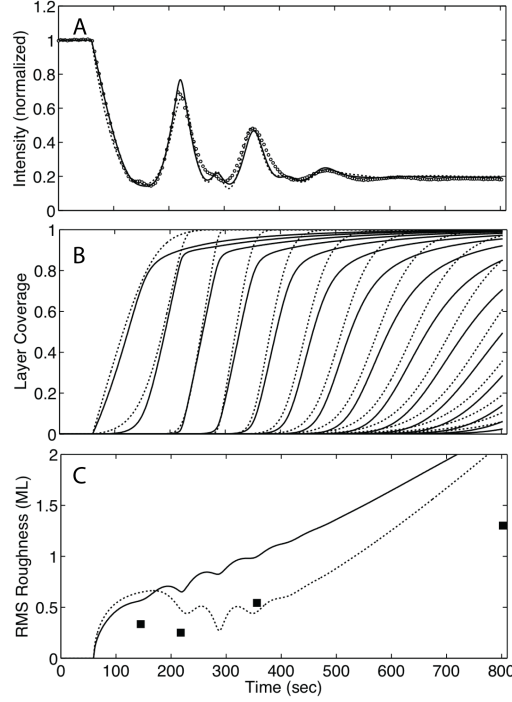


FIG. 10: a) (open circles) X-ray reflectivity data obtained near the DIP anti-Bragg position during DIP deposition on SiO_2 . Also shown are best-fit curves from two of the models described in the text, the modified Cohen model (solid line), and the Braun/Kaganer model (dashed line). b) Layer coverages from the two models shown in (a). b) Lines show the evolution of root-mean square roughness obtained from the three models shown in (a) and (b). Filled squares are measured rms roughness values obtained from ex situ AFM.

was performed in part at the Cornell High Energy Synchrotron Source, also supported by the National Science Foundation and NIH-NIGMS (NSF-DMR-0225180). JRE acknowledges supplementary support via NSF-ECS-0210693 and NSF-ECS-0304483.

¹ J. H. Neave, P. J. Dobson, B. A. Joyce, and J. Zhang, Appl. Phys. Lett. **47**, 100 (1985).

² P. I. Cohen, P. R. Pukite, J. M. Vanhove, and C. S. Lent, J. Vac. Sci. Techn. A **4**, 1251 (1986).

³ P. H. Fuoss, D. W. Kisker, F. J. Lamelas, G. B. Stephenson, P. Imperatori, and S. Brennan, Phys. Rev. Lett. **69**, 2791 (1992).

⁴ O. M. Magnussen, K. Krug, A. H. Ayyad, and J. Stettner, Electrochim. Acta **53**, 3449 (2008).

⁵ M. V. R. Murty, T. Curcic, A. Judy, B. H. Cooper, A. R. Woll, J. D. Brock, S. Kycia, and R. L.

- Headrick, Phys. Rev. B **60**, 16956 (1999).
- ⁶ G. B. Stephenson, J. A. Eastman, C. Thompson, O. Auciello, L. J. Thompson, A. Munkholm, P. Fini, S. P. DenBaars, and J. S. Speck, Appl. Phys. Lett. **74**, 3326 (1999).
 - ⁷ M. Lippmaa, N. Nakagawa, M. Kawasaki, S. Ohashi, and H. Koinuma, Appl. Phys. Lett. **76**, 2439 (2000).
 - ⁸ G. Eres, J. Z. Tischler, M. Yoon, B. C. Larson, C. M. Rouleau, D. H. Lowndes, and P. Zschack, Appl. Phys. Lett. **80**, 3379 (2002).
 - ⁹ A. Fleet, D. Dale, Y. Suzuki, and J. D. Brock, Phys. Rev. Lett. **94**, (2005).
 - ¹⁰ A. Fleet, D. Dale, A. R. Woll, Y. Suzuki, and J. D. Brock, Phys. Rev. Lett. **96**, (2006).
 - ¹¹ J. Tischler, G. Eres, B. Larson, C. M. Rouleau, P. Zschack, and D. H. Lowndes, Phys. Rev. Lett. **96**, (2006).
 - ¹² D. Dale, Y. Suzuki, and J. D. Brock, J. Phys.: Condens. Matter **20**, (2008).
 - ¹³ H. A. Vandervegt, H. M. Vanpinxteren, M. Lohmeier, E. Vlieg, and J. M. C. Thornton, Phys. Rev. Lett. **68**, 3335 (1992).
 - ¹⁴ A. R. Woll, R. L. Headrick, S. Kycia, and J. D. Brock, Phys. Rev. Lett. **83**, 4349 (1999).
 - ¹⁵ W. Braun, B. Jenichen, V. M. Kaganer, A. G. Shtukenberg, L. Daweritz, and K. H. Ploog, Surf. Sci. **525**, 126 (2003).
 - ¹⁶ S. Kowarik, A. Gerlach, W. Leitenberger, J. Hu, G. Witte, C. Woll, U. Pietsch, and F. Schreiber, Thin Solid Films **515**, 5606 (2007).
 - ¹⁷ S. Kowarik, A. Gerlach, and F. Schreiber, J. Phys.: Condens. Matter **20**, (2008).
 - ¹⁸ S. Kowarik, A. Gerlach, M. W. A. Skoda, S. Sellner, and F. Schreiber, Eur. Phys. J. Spec. Top. **167**, 11 (2009).
 - ¹⁹ S. Kowarik, A. Gerlach, S. Sellner, L. Cavalcanti, and F. Schreiber, Adv. Eng. Mater. **11**, 291 (2009).
 - ²⁰ A. Amassian, T. V. Desai, S. Kowarik, S. Hong, A. R. Woll, G. G. Malliaras, F. Schreiber, and J. R. Engstrom, J. Chem. Phys. **130**, (2009).
 - ²¹ R. L. Headrick, S. Kycia, A. R. Woll, J. D. Brock, and M. V. R. Murty, Phys. Rev. B **58**, 4818 (1998).
 - ²² A. Amassian, V. A. Pozdin, T. V. Desai, S. Hong, A. R. Woll, J. D. Ferguson, J. D. Brock, G. G. Malliaras, and J. R. Engstrom, J. Mater. Chem. **19**, 5580 (2009).
 - ²³ T. W. Schroeder, Ph.D. thesis, Cornell University (2004).

- ²⁴ S. K. Sinha, E. B. Sirota, S. Garoff, and H. B. Stanley, Phys. Rev. B **38**, 2297 (1988).
- ²⁵ A. C. Mayer, R. Ruiz, R. L. Headrick, A. Kazimirov, and G. G. Malliaras, Org. Electron. **5**, 257 (2004).
- ²⁶ R. Ruiz, B. Nickel, N. Koch, L. C. Feldman, R. F. Haglund, A. Kahn, and G. Scoles, Phys. Rev. B **67**, (2003).
- ²⁷ A. C. Mayer, R. Ruiz, H. Zhou, R. L. Headrick, A. Kazimirov, and G. G. Malliaras, Phys. Rev. B **73**, (2006).
- ²⁸ S. T. Wo, B. R. Wang, H. Zhou, Y. P. Wang, J. Bessette, R. L. Headrick, A. C. Mayer, G. G. Malliaras, and A. Kazimirov, J. Appl. Phys. **100**, (2006).
- ²⁹ G. B. Stephenson, D. D. Fong, M. V. R. Murty, S. K. Streiffer, J. A. Eastman, O. Auciello, P. H. Fuoss, A. Munkholm, M. E. M. Aanerud, and C. Thompson, Physica B **336**, 81 (2003).
- ³⁰ M. G. Barthes and A. Rolland, Thin Solid Films **76**, 45 (1981).
- ³¹ C. Argile and G. E. Rhead, Surf. Sci. Reports **10**, 277 (1989).
- ³² A. Mroz and A. Mroz, Thin Solid Films **367**, 126 (2000).
- ³³ Q. Fu and T. Wagner, Phys. Rev. Lett. **90**, 4 (2003).
- ³⁴ I. T. Koponen, Nucl. Instrum. Methods B **171**, 314 (2000).
- ³⁵ J. Sillanpaa, I. T. Koponen, and N. Gronbech-Jensen, Nucl. Instrum. Methods B **184**, 523 (2001).
- ³⁶ T. Huhtamaki, M. O. Jahma, and I. T. Koponen, Nucl. Instrum. Methods B **264**, 55 (2007).
- ³⁷ P. I. Cohen, G. S. Petrich, P. R. Pukite, G. J. Whaley, and A. S. Arrott, Surf. Sci. **216**, 222 (1989).
- ³⁸ R. Kariotis and M. G. Lagally, Surf. Sci. **216**, 557 (1989).
- ³⁹ V. I. Trofimov, V. G. Mokerov, and A. G. Shumyankov, Thin Solid Films **306**, 105 (1997).
- ⁴⁰ V. I. Trofimov, J. Comm. Tech. Electron. **44**, 1246 (1999).
- ⁴¹ V. I. Trofimov and V. G. Mokerov, Thin Solid Films **428**, 66 (2003).
- ⁴² V. I. Trofimov, J. Kim, and S. Bae, Surf. Sci. **601**, 4465 (2007).
- ⁴³ V. I. Trofimov, J. Kim, and S. Bae, J. Phys. Conf. Ser. **100**, 082005 (2008).
- ⁴⁴ J. A. Venables, G. D. T. Spiller, and M. Hanbucken, Rep. Prog. Phys. **47**, 399 (1984).
- ⁴⁵ S. Hong, A. Amassian, A. R. Woll, S. Bhargava, J. D. Ferguson, G. G. Malliaras, J. D. Brock, and J. R. Engstrom, Appl. Phys. Lett. **92** (2008).
- ⁴⁶ K. Bromann, H. Brune, H. Roder, and K. Kern, Phys. Rev. Lett. **75**, 677 (1995).

- ⁴⁷ M. Tomellini and M. Fanfoni, J. Phys.: Condens. Matter **18**, 4219 (2006).
- ⁴⁸ J. D. Ferguson, G. Arikan, D. S. Dale, A. R. Woll, and J. D. Brock, Phys. Rev. Lett. **103**, 256103 (2009).
- ⁴⁹ R. Ruiz, D. Choudhary, B. Nickel, T. Toccoli, K. C. Chang, A. C. Mayer, P. Clancy, J. M. Blakely, R. L. Headrick, S. Iannotta, et al., Chem. Mater. **16**, 4497 (2004).
- ⁵⁰ W. H. Press, B. Flannery, S. A. Teukolsky, and W. T. Vetterling, *Numerical Recipes, The Art of Scientific Computing (Fortran Version)* (Cambridge University Press, New York, 1989).
- ⁵¹ S. E. Fritz, S. M. Martin, C. D. Frisbie, M. D. Ward, and M. F. Toney, J. Am. Chem. Soc. **126**, 4084 (2004).
- ⁵² S. Kowarik, A. Gerlach, S. Sellner, L. Cavalcanti, O. Konovalov, and F. Schreiber, Appl. Phys. A **95**, 233 (2009).
- ⁵³ S. K. Sinha, Y. P. Feng, C. A. Melendres, D. D. Lee, T. P. Russell, S. K. Satija, E. B. Sirota, and M. K. Sanyal, Physica A **231**, 99 (1996).
- ⁵⁴ The pentacene/SiO₂ films shown in Fig. 1 were subsequently re-used prior to this analysis, and hence could not be re-measured.